RSC Advances

PAPER

View Article Online
View Journal | View Issue

Cite this: *RSC Adv.*, 2024, **14**, 17434

Achievement of efficient thermally activated delayed fluorescence materials based on 1,8-naphthalimide derivatives exhibiting piezochromic and thermochromic luminescence†

Meiling Chen‡,[ab] Yuzhuo Chen‡,[cd] Zhongzhen Su,[cd] Yuchun Li,[e] Hanxiao Fei,[e] Hua Zhang*[e] and Yunan Wu*[fg]

Received 22nd April 2024
Accepted 24th May 2024

DOI: 10.1039/d4ra02981j

rsc.li/rsc-advances

In this study, we developed a D–A type imide derivative based on 1,8-naphthalimide, NI-mPCz, which exhibited outstanding thermally activated delayed fluorescence (TADF) properties. Additionally, it demonstrates characteristics of piezochromic and thermochromic luminescence. The thermochromic luminescence observed is attributed to crystalline transformations occurring during the heating process, as evidenced by differential scanning calorimetry (DSC) and microscopic examinations. Moreover, the good compatibility of NI-mPCz with HeLa cells and its excellent imaging performance indicate its potential for application in the field of biological imaging. These results provide valuable insights for the design and development of new organic electronic and bioimaging materials with high-efficiency TADF characteristics.

Introduction

In recent years, organic luminescent materials have garnered extensive attention due to their widespread applications in photonic devices,[1,2] sensors,[3,4] bioimaging,[5–7] and therapeutics.[8,9] Among these materials, thermally activated delayed fluorescence (TADF) materials have been particularly highlighted for their potential to achieve 100% internal quantum efficiency and to manufacture cost-effective organic light-emitting diodes (OLEDs).[10–18] However, the practical application of TADF materials is constrained by challenges related to material stability and the controllability of optoelectronic properties,[19–22] which are largely dependent on the polymorphic behavior and phase transition characteristics of the materials.

Stimuli-responsive materials can alter their physical and/or chemical properties in response to external stimuli or environmental changes.[23–25] The design and synthesis of molecules with such characteristics have garnered significant attention for the development of advanced sensing materials. Through in-depth study of the structures and response mechanisms of these materials, it is possible to design and develop novel stimuli-responsive materials with superior performance and broad application prospects. These materials not only have crucial applications in sensing, optoelectronic devices, and information storage but also provide valuable theoretical and practical insights for the design of future smart materials. By further optimizing molecular design and synthesis methodologies, it is feasible to achieve more efficient and multifunctional stimuli-responsive materials, thereby presenting new opportunities for scientific research and technological development.

The luminescent properties of materials vary with temperature, leading to changes in their crystal structure, optical, and electronic behaviors, which in turn affect their performance in practical applications. Therefore, studying the temperature's impact on polymorphism is crucial for understanding and optimizing the performance of TADF materials.[26–31] Despite increasing interest in the polymorphism of organic luminescent materials, there is still a lack of comprehensive understanding of the polymorphic transformation mechanisms of specific compounds and their effects on luminescent properties.

[a]*State Key Laboratory of Oncology in South China, Guangdong Provincial Clinical Research Center for Cancer, Sun Yat-sen University Cancer Center, Guangzhou 510060, China*

[b]*Department of Nuclear Medicine, Sun Yat-sen University Cancer Center, Guangzhou 510060, China*

[c]*Department of Ultrasound, The Fifth Affiliated Hospital, Sun Yat-sen University, Zhuhai 519000, China*

[d]*Department of Interventional Medicine, Guangdong Provincial Key Laboratory of Biomedical Imaging, The Fifth Affiliated Hospital, Sun Yat-sen University, Zhuhai 519000, China*

[e]*Shenzhen Key Laboratory of Systems Medicine for Inflammatory Diseases, School of Medicine, Shenzhen Campus of Sun Yat-Sen University, Sun Yat-sen University, Shenzhen, 518107, P. R. China. E-mail: zhangh255@mail.sysu.edu.cn*

[f]*Guangzhou Institute of Chemistry, Chinese Academy of Sciences, Guangzhou, 510650, P. R. China. E-mail: wuyunan@mail3.sysu.edu.cn*

[g]*Hengyang Aijie Technology Co, Ltd, Hengyang 421006, China*

† Electronic supplementary information (ESI) available. CCDC 2344999. For ESI and crystallographic data in CIF or other electronic format see DOI: https://doi.org/10.1039/d4ra02981j

Against this backdrop, 1,8-naphthalimide derivatives, as a class of important organic luminescent materials, have attracted widespread attention due to their excellent electronic and optical properties.[32–34] By finely tuning the molecular structure of these compounds, such as introducing different functional groups, their TADF characteristics can be effectively regulated to optimize their performance.[35–38]

Previously, our research team synthesized red-emitting TADF materials based on 1,8-naphthalimide derivatives.[39] In this study, We altered the electron-donating component to carbazole and successfully synthesized NI-mPCz, which exhibited blue–green TADF properties. Additionally, NI-mPCz exhibited piezochromic and thermochromic luminescence characteristics, attributed predominantly to the polymorphic transformations occurring within its crystalline framework upon heating. Moreover, considering the potential applications of TADF materials in bioimaging, we further explored the potential application of this compound in cell imaging. Our research not only provides new insights into the understanding and utilization of the polymorphism of TADF materials but also opens up new avenues for the design and optimization of high-performance TADF luminescent materials through crystal engineering, offering valuable guidance for their development in bioimaging and other advanced application fields.

Results and discussion

A novel NI derivative, NI-mPCz, was synthesized *via* an amide formation reaction and the Suzuki coupling (Scheme 1), as depicted in Fig. 1a. The compound's structure was characterized by ^{1}H NMR and ^{13}C NMR, electron ionization (EI), and high-resolution mass spectrometry (Fig. S1–S4†), and confirmed by single-crystal X-ray diffraction analysis. The crystal structure, illustrated in Fig. 1b, shows that NI-mPCz has a highly twisted configuration, with a dihedral angle of 54.9° between the NI unit and the bridging phenyl ring. This significant geometric distortion facilitates the effective separation of the molecule's HOMO and LUMO, further reducing the energy gap (ΔE_{ST}) and promoting delayed fluorescence. Time-dependent density functional theory (TD-DFT) calculations, as shown in Fig. 1c, further elucidate the crystal's conformation, demonstrating a clear separation between the HOMO and LUMO. The HOMO is predominantly localized on the carbazole moiety, while the LUMO is mainly located on the NI unit, resulting in minimal orbital overlap. The calculated ΔE_{ST} for this structure is 0.34 eV, which is essential for efficient reverse intersystem crossing (RISC) and TADF emission. The HOMO and LUMO energy levels of NI-mPCz are calculated to be −5.83 eV and −2.83 eV, respectively.

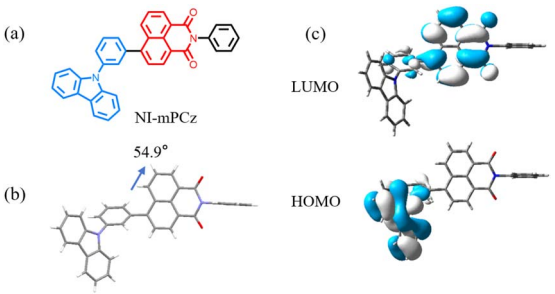

Fig. 1 (a) Molecular structures of NI-mPCz. (b) Crystal structures of NI-mPCz (CCDC 2344999). (c) The HOMO and LUMO orbital distributions of NI-mPCz on TD-DFT at the B3LYP functional and 6-31G(d) basis.

The photophysical properties of NI-mPCz were thoroughly examined, including its ultraviolet-visible (UV-vis) absorption, fluorescence, and phosphorescence characteristics. As illustrated in Fig. 2a, the UV-vis absorption spectrum of NI-mPCz in tetrahydrofuran (THF) solution shows pronounced absorption bands between 275–306 nm, attributable to the π–π* transitions of the locally excited (LE) state. The strong absorption from 306–400 nm is associated with intramolecular charge transfer (ICT) transitions. Molecules with a donor–acceptor (D–A) structure in their excited state typically possess a relatively large dipole moment, rendering them sensitive to solvent polarization effects. Consequently, they may exhibit different luminescence behaviors in solvents of varying polarities, displaying a trend of red-shifting emission wavelengths with

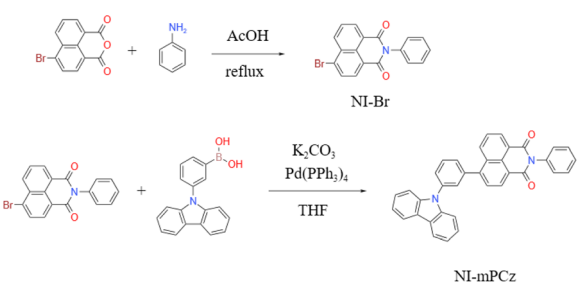

Scheme 1 Synthetic route of NI-mPCz.

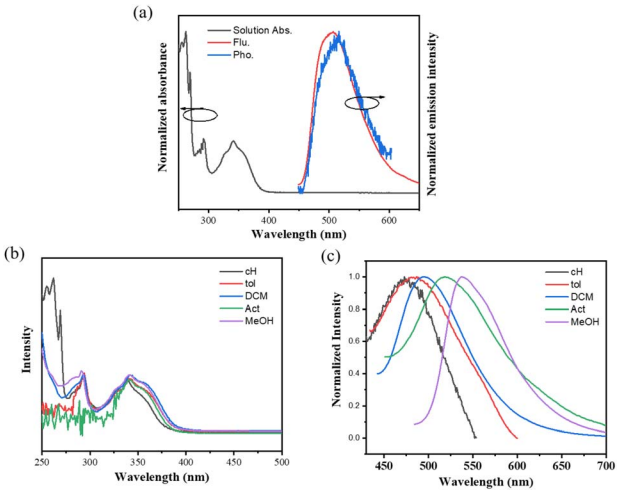

Fig. 2 (a) Normalized solution absorption in tetrahydrofuran (Solution Abs. $c = 10^{-5}$ M), fluorescence (Flu., solid state) and phosphorescence (Pho., solid state at 77 K) spectra (excitation wavelength: 365 nm) of NI-mPCz; (b) normalized solution absorption ($c = 10^{-5}$ M); (c) normalized solution fluorescence ($c = 10^{-5}$ M) of NI-mPCz in different solvents.

increasing solvent polarity. The photophysical properties of NI-mPCz were probed in solvents with different polarities (concentration $c = 10^{-5}$ M), including cyclohexane (cH), toluene (tol), dichloromethane (DCM), acetone (Act), and methanol (MeOH), and both its UV-vis absorption and fluorescence spectra were obtained. As depicted in Fig. 2b and c, the UV-vis absorption spectra of NI-mPCz are fairly consistent across various solvents. The fluorescence spectra exhibit a red shift with the increase in solvent polarity, indicating that the dipole moment of the excited state increases with the solvent's polarity, thereby confirming that the emission originates from intramolecular charge transfer. The ΔE_{ST} in the solid state was determined from the onset wavelengths of the fluorescence and phosphorescence spectra, with the ΔE_{ST} value of NI-mPCz calculated to be 0.03 eV. Such a small ΔE_{ST} value is conducive to efficient RISC processes, favoring highly emissive TADF in the solid state.

The photoluminescence spectra of NI-mPCz powder were measured in the range of 100–300 K. As shown in Fig. 3a, the photoluminescence intensity of NI-mPCz increases with the rising temperature from 100 K to 300 K. The emission lifetime of NI-mPCz was investigated, revealing the presence of an additional long-lived emission component in its fluorescence decay curve in the solid state, as illustrated in Fig. 3. Notably, the excited-state lifetime of NI-mPCz at 300 K was measured to be 14.96 μs. Furthermore, the long-lived component in NI-mPCz's fluorescence decay curve shows a gradual increase with rising temperature. These findings provide evidence for the existence of TADF in these materials.

The stimulus-responsive fluorescence properties of the solid-state NI-mPCz were further investigated. As illustrated in Fig. 4a, the luminescence color of NI-mPCz powder changes from blue to green after being subjected to mechanical stimulation, with the emission wavelength shifting from 499 nm to 524 nm. This red shift in mechanoluminescence is likely caused by the disruption of the crystal structure, resulting in decreased crystallinity, reduced intermolecular spacing, and enhanced π–π interactions.

Upon examining the effects of temperature on the luminescence properties of NI-mPCz, As shown in Fig. 4b, it is observed that the emission wavelength undergoes multiple shifts with increasing temperature. Differing from conventional thermally-induced chromatic transitions in luminescent materials, which typically exhibit unidirectional red or blue shifts, NI-mPCz

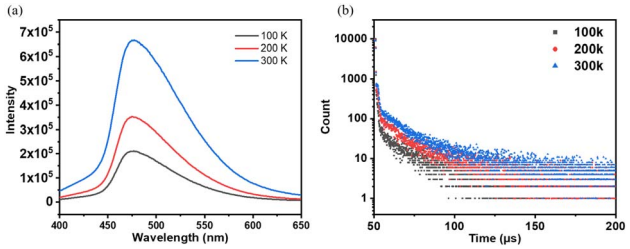

Fig. 3 (a) Fluorescence spectrum and (b) fluorescence intensity decay curve of the solid state of NI-mPCz at different temperatures.

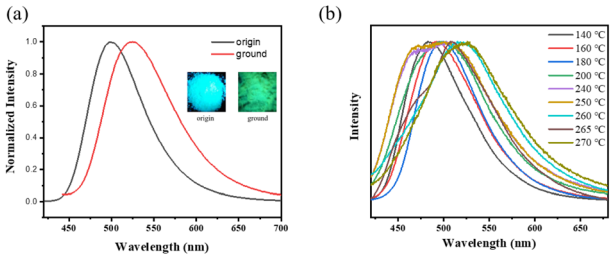

Fig. 4 (a) The luminescence spectra of origin and ground powder; (b) the luminescence spectra of NI-mPCz powder at various temperatures.

demonstrates a complex thermochromic behavior. Specifically, the emission spectrum shifts from red to blue, and then back to red again, over a temperature range from 140 °C to 270 °C.

To provide a reasonable explanation for this issue, we conducted differential scanning calorimetry (DSC) measurements to investigate the possible phase transition processes related to temperature changes. The DSC curve shows three distinct endothermic peaks, indicating multiple thermal transitions (refer to Table 1 and Fig. 5b). This observation suggests that during heating, NI-mPCz undergoes a series of melting and recrystallization events, indicating the presence of various crystalline forms that can interconvert through thermal treatment. As depicted in Fig. 5a, TGA analysis of NI-mPCz reveals a mass loss at 160 °C, aligning with the first melting peak

Table 1 The thermal conversion temperature of NI-mPCz

Tg (°C)	Tm_1 (°C)	Tm_2 (°C)	Tm_3 (°C)
135	164	249	278

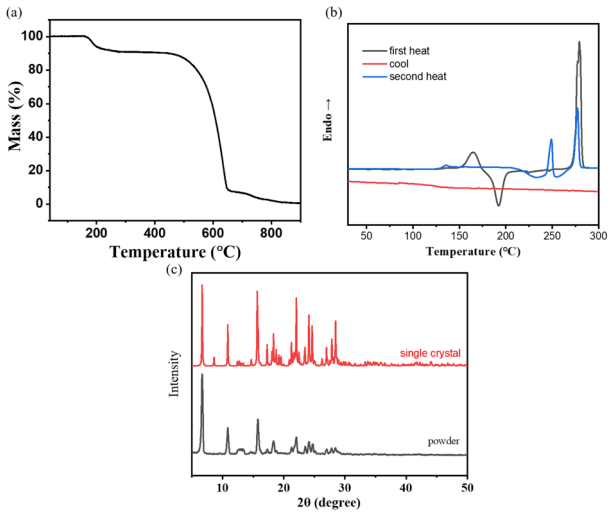

Fig. 5 (a) The thermogravimetric analysis and (b) the differential scanning calorimetry curves of NI-mPCz; (c) the XRD curve of single crystal and powder.

observed in the DSC analysis, suggesting partial decomposition at this temperature. Comparative analysis of powder X-ray diffraction (PXRD) and single-crystal X-ray diffraction (SCXRD) results revealed similar diffraction patterns (as shown in Fig. 5c), suggesting that the powder and single-crystal forms have similar crystal structures. The single-crystal structure of NI-mPCz contains dichloromethane molecules, which are released from the crystal upon heating to approximately 164 °C, resulting in a transition from crystal form I to form II. At 249 °C, crystal form II melts, followed by recrystallization between 260–270 °C to form crystal form III. Finally, at 278 °C, crystal form III melts, transitioning to an amorphous state.

To further explore the thermal behavior of NI-mPCz, we utilized microscopy to observe its crystalline state changes during the heating process, as shown in the Fig. 6. Within the temperature range of 160 °C to 170 °C, NI-mPCz noticeably transitions from a crystalline to a molten state. At 180 °C, the compound reverts to its crystalline state. As the temperature rises to 240 °C, melting begins to occur, and by 250 °C, the proportion of the crystalline state increases. When the temperature reaches 260 °C, the melting becomes more pronounced, indicating that the compound has started to melt. These findings clearly illustrate the multiple polymorphic transformations of NI-mPCz throughout the heating process.

Therefore, it is evident that the spectral transformations observed in NI-mPCz during the heating process are attributable to multiple polymorphic transitions. As illustrated in Fig. 4b, in the temperature range from 140 °C to 240 °C, the emission wavelength of NI-mPCz progressively shifts towards the red. This shift is primarily due to the gradual degradation of the crystalline structure, resulting in denser molecular packing and intensified π–π interactions, which culminate in the noted red-shifted luminescence. At 250 °C, NI-mPCz exhibits two prominent emission peaks at 469 nm and 503 nm, indicating that alongside the disintegration of the existing crystalline framework, a new crystalline phase emerges, characterized by blue-shifted emission peaks. Upon reaching 260 °C, the emission peak advances to 517 nm, signaling the onset of instability within the crystal phase formed at 250 °C. At 265 °C, the emission peak shifts further to 508 nm, with an additional shoulder peak appearing at 479 nm, suggesting the formation of a novel crystalline phase. Ultimately, at 270 °C, the emission peak transitions to 525 nm, marking the crystalline form developed at 265 °C transforming into an amorphous state. These findings underscore the intricate relationship between thermally induced structural changes and the luminescent properties of NI-mPCz, emphasizing the potential of such materials in applications that demand tunable emission properties.

Thermally responsive luminescence is a fascinating phenomenon realized through heating and cooling, with significant applications in anti-counterfeiting, luminescent thermometers, and thermal sensors due to its inherent advantages of non-invasiveness, high sensitivity, and *in situ* monitoring.[40–42] The majority of thermochromic luminescent materials reported in the literature are derived from temperature-dependent structural relaxation or conformational changes in the excited state. These materials exhibit pronounced changes in luminescent properties in response to temperature variations, enabling a wide range of applications. However, studies on temperature-induced crystalline phase transitions remain relatively scarce. Such phase transitions typically entail substantial alterations in crystal structure, which can profoundly affect the optical and electronic properties of the materials. Our research offers valuable insights into the luminescence changes associated with crystalline phase transitions during heating. By thoroughly investigating these transformation mechanisms, we can develop more efficient and multifunctional thermochromic luminescent materials, thereby creating new opportunities for scientific research and technological advancement.

Given its extended luminescence lifetime, NI-mPCz may be advantageous for applications in biological imaging, where it could significantly diminish interference from ambient fluorescence. By utilizing a self-assembly method, NI-mPCz was efficiently encapsulated within F127 polymer materials to form stable nanoparticles. These nanoparticles were subsequently introduced into the interior of cells through the mechanism of endocytosis. As shown in Fig. 7, under bright-field microscopy, the position of HeLa cells can be clearly observed. When switching to the blue fluorescence channel, a bright blue fluorescence signal can be seen emanating from within the cells, indicating that the nanoparticles containing NI-mPCz not only successfully entered the cells but also achieved effective light emission inside the cells. This result demonstrates the potential application of NI-mPCz nanoparticles in the field of biological imaging, providing a valuable tool for further biomedical research.

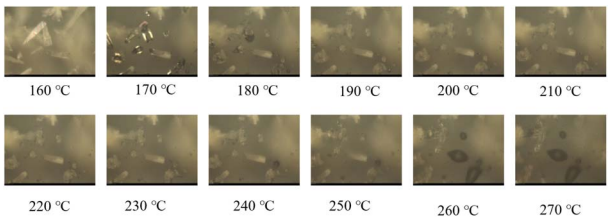

Fig. 6 Microscopic photographs of NI-mPCz at different temperatures.

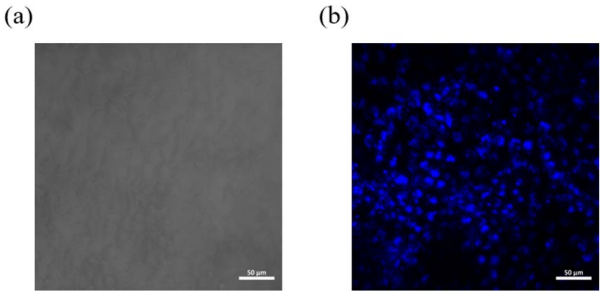

Fig. 7 (a) A bright field image of HeLa cells; (b) an image of HeLa cells under the blue light channel.

Experimental

Materials

6-Bromobenzo[de]isochromene-1,3-dione, aniline, palladium acetate, potassium carbonate and (3-(9*H*-carbazol-9-yl)phenyl) boronic acid were purchased from Aldrich. The other reagent were purchased from Guangzhou Jincheng company. All the materials and reagent were used as received.

Instrumentation

Hydrogen and carbon nuclear magnetic resonance spectra (^{1}HNMR and ^{13}CNMR) were recorded on a Bruker Avance III NMR spectrometer using deuterated dimethyl sulfoxide as the solvent and tetramethylsilane (TMS) as the internal reference. Mass spectrometry analyses, including low-resolution electron impact mass spectrometry (EI-MS) and high-resolution electron impact mass spectrometry (EI-HRMS), were performed on Thermo DSQ and Thermo MAT95XP instruments, respectively. Ultraviolet-visible (UV-vis) absorption spectra were obtained using a Hitachi U-3900 spectrophotometer, while photoluminescence (PL) spectra were acquired with an Ocean Optics QE65 Pro spectrometer. Fluorescence lifetimes, temperature-dependent lifetimes, time-resolved spectra, and fluorescence quantum efficiencies were measured using a Horiba JY FL-3 combined steady-state/transient fluorescence spectrometer equipped with a calibrated integrating sphere for quantum efficiency assessments. Thermal properties were examined using a Shimadzu TGA-50H thermogravimetric analyzer at a heating rate of 20 °C min^{-1} and a NETZSCH DSC 204 F1 differential scanning calorimeter at a heating rate of 10 °C min^{-1}, both under a nitrogen atmosphere. Density Functional Theory (DFT) calculations were performed with the Gaussian 09W program employing the B3LYP/6-31G(d) method and basis set, and Time-Dependent Density Functional Theory (TD-DFT) calculations were based on the B3LYP/6-31G(d) method. X-ray powder diffraction measurements were conducted using a Rigaku Miniflex600 instrument. Optical microscopy examinations were performed with a Leica Microsystems DM2700P microscope. X-ray single crystal diffraction analysis was carried out using a Super Nova single crystal diffractometer. For cell imaging studies, observations were made using a confocal microscope.

Synthesis

6-Bromo-2-phenyl-1*H*-benzo[de]isoquinoline-1,3-(2*H*)-dione (NI–Br). In a typical procedure, a mixture of 4-bromo-1,8-naphthalic anhydride (2.77 g, 10 mmol) and aniline (1.1 g, 11.8 mmol) was dissolved in 100 mL of acetic acid in a reaction flask. The solution was refluxed overnight under an argon atmosphere. After completion of the reaction, the mixture was poured into 300 mL of water to precipitate the product. The solid was then isolated by filtration and dried to obtain the final product without further purification.[39]

6-(3-(9*H*-Carbazol-9-yl)phenyl)-2-phenyl-1*H*-benzo[de]isoquino-line-1,3(2*H*)-dione (NI-mPCz). A reaction mixture comprising NI–Br (0.5 g, 1.42 mmol) and (3-(9*H*-carbazol-9-yl) phenyl)boronic acid (0.61 g, 2.13 mmol) was introduced into a round-bottom flask and solubilized in 100 mL of tetrahydrofuran. Subsequently, the solution was agitated under an inert argon atmosphere for 30 minutes, after which an aqueous solution of potassium carbonate (1.5 g dissolved in 3 mL of water) was added, followed by the introduction of 0.02 g of $Pd(Ph_3)_4$ as a catalyst. The reaction mixture was then subjected to reflux under an argon blanket for a duration of 6 hours. Upon cooling to ambient temperature, the reaction mixture was diluted with 50 mL of water and subjected to liquid–liquid extraction using methylene chloride, performed thrice. The combined organic extracts were dried over anhydrous sodium sulfate, filtered, and the solvent was removed under reduced pressure. The resulting crude product was subjected to purification *via* column chromatography on silica gel, employing a mixture of dichloromethane and hexane (v/v = 1/2) as the mobile phase. This purification process yielded 0.64 g of the desired product NI-mPCz, corresponding to a yield of 88%. ^{1}H NMR (500 MHz, DMSO) 8.57 (1*H*, d, *J* 7.5), 8.48 (1*H*, d, *J* 8.4), 8.27 (1*H*, d, *J* 7.7), 8.01 (1*H*, d, *J* 7.5), 7.99–7.91 (1*H*, m), 7.86 (1*H*, d, J 8.1), 7.81 (0*H*, s), 7.75 (1*H*, d, *J* 7.6), 7.56 (2*H*, dd, *J* 15.0, 7.9), 7.48 (2*H*, t, *J* 7.7), 7.41 (1*H*, d, *J* 7.2), 7.32 (1*H*, t, *J* 7.3). ^{13}C NMR (126 MHz, DMSO) δ 164.15, 163.92, 145.42, 140.69, 140.54, 137.88, 136.43, 132.66, 131.33, 131.17, 130.83, 129.89, 129.57, 129.35, 128.87, 128.71, 128.25, 128.15, 127.30, 126.86, 123.54, 123.34, 122.72, 121.05, 120.72, 110.20, 40.50, 40.33, 40.16, 40.00, 39.83, 39.66, 39.49. HRMS, *m*/*z*: [M] + calcd for $C_{36}H_{24}N_2O_2$, 514.1681; found, 514.1673.

Conclusions

In this study, we synthesized and characterized the D–A type imide derivative NI-mPCz, featuring a robust electron-accepting 1,8-naphthalimide unit and a non-planar, potent electron-donating carbazole unit, demonstrating pronounced TADF properties. NI-mPCz exhibits unique thermochromic luminescence, distinct from traditional thermochromic luminescent materials, as it does not show a straightforward unidirectional red or blue shift upon heating. Instead, between 140 °C and 270 °C, its emission spectrum undergoes sequential shifts: initially red, followed by blue, and then reverting to red. Through DSC analysis, we examined the endothermic and exothermic behaviors during the heating process, and microscopic investigations revealed multiple transitions between crystalline states, suggesting complex thermal behavior and phase transitions in NI-mPCz. Although the complete single-crystal structure of NI-mPCz eluded us, our research provides a novel example for understanding piezochromic and thermofluorochromism. Through further optimization of molecular design and synthesis methods, we can develop more efficient and multifunctional stimuli-responsive materials, thereby creating new opportunities for scientific research and technological advancement. Additionally, the good compatibility of NI-mPCz with HeLa cells and the excellent imaging results indicate the potential of this material in the field of biological imaging. These findings provide valuable insights for the development of new organic electronic and bioimaging materials with efficient TADF properties.

Author contributions

The experiments were designed by Yunan Wu and Hua Zhang. Meiling Chen, Yuzhuo Chen, Zhongzhen Su, Yuchun Li, Hanxiao Fei, Hua Zhang, and Yunan Wu conducted the experiments. Yunan Wu drafted the manuscript. All authors contributed to the analysis and interpretation of the data.

Conflicts of interest

There are no conflicts to declare.

Acknowledgements

This work was supported by the National Key Research and development program of China (2022YFC2305400), the National Natural Science Foundation of China (82372246, 81872224), Guangdong Basic and Applied Basic Research Foundation (2021A1515010734), Shenzhen Science and Technology Program (JCYJ20230807111219040, JCYJ20190807153211194, ZDSYS20220606100803007).

References

1 J. Jayabharathi, A. Prabhakaran, V. Thanikachalam and M. Sundharesan, *RSC Adv.*, 2016, **6**, 62208–62217.
2 M. Xu, X. Li, S. Liu, L. Zhang and W. Xie, *Mater. Chem. Front.*, 2023, **7**, 4744–4767.
3 K. Chen and C. Wu, *Chin. Chem. Lett.*, 2018, **29**, 823–826.
4 Y. Zhao and D. Li, *J. Mater. Chem. C*, 2020, **8**, 12739–12754.
5 W. Li, Z. Liang, P. Wang and Q. Ma, *Biosens. Bioelectron.*, 2024, **249**, 116008.
6 X. Li, S. Lu, D. Tu, W. Zheng and X. Chen, *Nanoscale*, 2020, **12**, 15021–15035.
7 E. Kamya, Z. Lu, Y. Cao and R. Pei, *J. Mater. Chem. B*, 2022, **10**, 9770–9788.
8 X. Y. Lou, G. Zhang, N. Song and Y. W. Yang, *Biomaterials*, 2022, **286**, 121595.
9 L. Hu, C. Xiong, J. J. Zou, J. Chen, H. Lin, S. J. Dalgarno, H. C. Zhou and J. Tian, *ACS Appl. Mater. Interfaces*, 2023, **15**, 25369–25381.
10 J. Liang, C. Li, Y. Cui, Z. Li, J. Wang and Y. Wang, *J. Mater. Chem. C*, 2020, **8**, 1614–1622.
11 N. N. T. Nguyen, H. Mubarok, T. Lee, T. Q. Tran, J. Jung and M. H. Lee, *RSC Adv.*, 2022, **12**, 29892–29899.
12 B. Ashwood, M. Pollum and C. E. Crespo-Hernandez, *Photochem. Photobiol.*, 2019, **95**, 33–58.
13 G. Mehes, H. Nomura, Q. Zhang, T. Nakagawa and C. Adachi, *Angew. Chem., Int. Ed.*, 2012, **51**, 11311–11315.
14 Q. Zhang, J. Li, K. Shizu, S. Huang, S. Hirata, H. Miyazaki and C. Adachi, *J. Am. Chem. Soc.*, 2012, **134**, 14706–14709.
15 Q. T. Siddiqui, A. A. Awasthi, P. Bhui, P. Parab, M. Muneer, S. Bose and N. Agarwal, *RSC Adv.*, 2019, **9**, 40248–40254.
16 G. Xiao, Y.-J. Ma, Z. Qi, X. Fang, T. Chen and D. Yan, *Chem. Sci.*, 2024, **15**, 3625–3632.
17 B. Zhou, Z. Qi, M. Dai, C. Xing and D. Yan, *Angew. Chem., Int. Ed.*, 2023, **62**, e202309913.
18 B. Zhou, G. Xiao and D. Yan, *Adv. Mater.*, 2021, **33**, 2007571.
19 D. Zhang, M. Cai, Y. Zhang, D. Zhang and L. Duan, *Mater. Horiz.*, 2016, **3**, 145–151.
20 X. L. Chen, X. D. Tao, Z. Wei, L. Meng, F. L. Lin, D. H. Zhang, Y. Y. Jing and C. Z. Lu, *ACS Appl. Mater. Interfaces*, 2021, **13**, 46909–46918.
21 Y. Zhang, D. Zhang, T. Tsuboi, Y. Qiu and L. Duan, *Sci. China: Chem.*, 2019, **62**, 393–402.
22 J. Chen, Z. Liu, L. Chen, P. Zou, B. Z. Tang and Z. Zhao, *Small*, 2024, **20**, e2306800.
23 C. Xing, Z. Qi, B. Zhou, D. Yan and W.-H. Fang, *Angew. Chem., Int. Ed.*, 2024, **63**, e202402634.
24 C. Xing, B. Zhou, D. Yan and W.-H. Fang, *CCS Chem.*, 2023, **5**, 2866–2876.
25 C. Xing, B. Zhou, D. Yan and W.-H. Fang, *Adv. Sci.*, 2024, **11**, 2310262.
26 K. Zheng, F. Ni, Z. Chen, C. Zhong and C. Yang, *Angew. Chem., Int. Ed.*, 2020, **59**, 9972–9976.
27 S. Li, L. Fu, X. Xiao, H. Geng, Q. Liao, Y. Liao and H. Fu, *Angew. Chem., Int. Ed.*, 2021, **60**, 18059–18064.
28 Y. Zhou, L. Qian, M. Liu, X. Huang, Y. Wang, Y. Cheng, W. Gao, G. Wu and H. Wu, *J. Mater. Chem. C*, 2017, **5**, 9264–9272.
29 Y. Chen, X. Zhang, M. Wang, J. Peng, Y. Zhou, X. Huang, W. Gao, M. Liu and H. Wu, *J. Mater. Chem. C*, 2019, **7**, 12580–12587.
30 S. Ito, *CrystEngComm*, 2022, **24**, 1112–1126.
31 B. P. Mali, S. R. Dash, A. Biswas, K. Vanka, K. Manoj and R. G. Gonnade, *Cryst. Growth Des.*, 2022, **22**, 1892–1905.
32 H. Sun, L. Wang, Y. Wang and X. Guo, *Chemistry*, 2019, **25**, 87–105.
33 Q.-H. Ling, J.-L. Zhu, Y. Qin and L. Xu, *Mater. Chem. Front.*, 2020, **4**, 3176–3189.
34 C. Li, Z. Lin, Y. Li and Z. Wang, *Chem. Rec.*, 2016, **16**, 873–885.
35 Y. Tsuji, N. Kanno, C. Goto, S. Katao, Y. Okajima, P. Reine, P. Imbrasas, S. Reineke, K. Shizu, T. Nakashima, H. Kaji, T. Kawai and M. Louis, *J. Mater. Chem. C*, 2023, **11**, 5968–5978.
36 K. Bartkowski, P. Zimmermann Crocomo, M. A. Kochman, D. Kumar, A. Kubas, P. Data and M. Lindner, *Chem. Sci.*, 2022, **13**, 10119–10128.
37 S. A. Elgadi, Y. Cai and Z. M. Hudson, *J. Mater. Chem. C*, 2023, **11**, 11589–11596.
38 H. F. Higginbotham, P. Pander, R. Rybakiewicz, M. K. Etherington, S. Maniam, M. Zagorska, A. Pron, A. P. Monkman and P. Data, *J. Mater. Chem. C*, 2018, **6**, 8219–8225.
39 M. Chen, Y. Chen, Y. Li, Y. Lin and Y. Wu, *RSC Adv.*, 2024, **14**, 6494–6500.
40 M. Liu, L. Zhai, J. Sun, P. Xue, P. Gong, Z. Zhang, J. Sun and R. Lu, *Dyes Pigm.*, 2016, **128**, 271–278.
41 B. Xu, Z. Song, M. Zhang, Q. Zhang, L. Jiang, C. Xu, L. Zhong, C. Su, Q. Ban, C. Liu, F. Sun, Y. Zhang, Z. Chi, Z. Zhao and G. Shi, *Chem. Sci.*, 2021, **12**, 15556–15562.
42 K. Yuhara and K. Tanaka, *Angew. Chem., Int. Ed.*, 2024, **63**, e202319712.